Energy release and transfer in guide field reconnection

J. Birn[1,a)] and M. Hesse[2]
[1]*Los Alamos National Laboratory, Los Alamos, New Mexico 87545, USA*
[2]*NASA/Goddard Space Flight Center, Greenbelt, Maryland 20771, USA*

(Received 1 December 2009; accepted 7 January 2010; published online 26 January 2010)

Properties of energy release and transfer by magnetic reconnection in the presence of a guide field are investigated on the basis of 2.5-dimensional magnetohydrodynamic (MHD) and particle-in-cell (PIC) simulations. Two initial configurations are considered: a plane current sheet with a uniform guide field of 80% of the reconnecting magnetic field component and a force-free current sheet in which the magnetic field strength is constant but the field direction rotates by 180° through the current sheet. The onset of reconnection is stimulated by localized, temporally limited compression. Both MHD and PIC simulations consistently show that the outgoing energy fluxes are dominated by (redirected) Poynting flux and enthalpy flux, whereas bulk kinetic energy flux and heat flux (in the PIC simulation) are small. The Poynting flux is mainly associated with the magnetic energy of the guide field which is carried from inflow to outflow without much alteration. The conversion of annihilated magnetic energy to enthalpy flux (that is, thermal energy) stems mainly from the fact that the outflow occurs into a closed field region governed by approximate force balance between Lorentz and pressure gradient forces. Therefore, the energy converted from magnetic to kinetic energy by Lorentz force acceleration becomes immediately transferred to thermal energy by the work done by the pressure gradient force. Strong similarities between late stages of MHD and PIC simulations result from the fact that conservation of mass and entropy content and footpoint displacement of magnetic flux tubes, imposed in MHD, are also approximately satisfied in the PIC simulations. © *2010 American Institute of Physics*. [doi:10.1063/1.3299388]

I. INTRODUCTION

Magnetic reconnection is considered the fundamental process underlying the energy release occurring, for instance, in solar flares and magnetospheric substorms. This release process consists primarily of the conversion of magnetic energy contained in stressed magnetic fields into particle kinetic energy. Traditionally the basics of magnetic reconnection have been studied in two-dimensional (2D) configurations, neglecting the dependence on one Cartesian coordinate (here chosen to be the y coordinate) with and without an initial magnetic field component in the y direction ("guide field"). Classical, resistive, magnetohydrodynamic (MHD) models (e.g., the linear tearing model of Furth *et al.*[1] and the steady-state model of Petschek[2]) show no dependence of the reconnection rate or mode structure on the magnitude of the guide field. In these models incompressibility was also assumed. Often, the presence of a strong guide field, for instance in many laboratory experiments, is taken as reason to justify an incompressibility approach (e.g., Ref. 3). However, for small or moderate guide fields this assumption need not be satisfied.

Previous investigations of the role of a guide field have focused mainly on the influence on the reconnection rate (e.g., Refs. 4–9), which might also be relevant for where and when reconnection is initiated, or on the spatial structure and dissipation physics (e.g., Refs. 4, 6, and 10–13). In this paper we focus on two other aspects of the role of a guide field: (1) the influence on energy transfer and dissipation and (2) the effect on the late configuration which involves the investigation of the validity of global constraints that might influence the accessibility and structure of the late states. The basis for these investigations is the configuration of the so-called "Newton challenge" problem,[14] generalized to include a guide field. In this approach, reconnection is initiated in a plane current sheet through a finite compression resulting from spatially and temporally limited plasma inflow (equivalent to an indentation of the boundaries).

2D simulations that include a guide field in the initial current sheet mostly assume uniform B_y, which does not affect the balance between finite plasma pressure inside the current sheet and the magnetic pressure of the reconnecting field component (here, B_x). This seems justified for studies of the influence on reconnection rate and the physics of reconnection, which may be influenced primarily by the magnitude of B_y at the x-line or separator. However, in low-β plasmas such as the solar corona, current sheets tend to be force-free or nearly force-free, such that current density and magnetic field vectors are nearly parallel or antiparallel. In such current sheets the magnetic pressure associated with B_x is balanced by the magnetic pressure $B_y^2/2\mu_0$ inside the current sheet and the strength of the guide field decreases from the center of the current sheet toward the outside. Such configurations are consistent with uniform plasma pressure which may be significantly lower than the magnetic pressure. This may have significant effects on the energy transfer, as demonstrated recently in Ref. 15. We will therefore consider both force-free initial states and current sheets with uniform B_y.

a)Electronic mail: jbirn@lanl.gov.

TABLE I. Initial parameters for seven PIC runs.

Run	guide field	T_e/T_i	m_e/m_i	β	N	$n_x \times n_z$
0	0	1/5	1/25	0.2	2.5×10^7	400×200
A1	0.8	1/5	1/25	0.2	5×10^7	400×400
A2	0.8	1	1/25	0.2	2.5×10^7	400×200
B1	Force-free	1/5	1/25	0.25	2.5×10^7	400×200
B2	Force-free	1	1/25	0.25	2.5×10^7	400×200
B3	Force-free	1/5	1/100	0.25	1×10^8	800×400
C	Force-free	1/5	1/25	1.00	2.5×10^8	400×400

In the following Sec. II we describe the initial states and the numerical approach. Section III then illustrates some characteristics of the dynamic evolution, following the onset of reconnection. Section IV demonstrates characteristic results on the energy transfer and dissipation, and Sec. V provides results on the validity of the global conservation laws and the characteristics of the late near-equilibrium states. In Sec. VI we then look for non-MHD effects in the particle-in-cell (PIC) simulations, specifically, anisotropy of the particle pressures and characteristics of velocity distributions in the outflow regions.

II. INITIAL STATES AND NUMERICAL APPROACHES

In the following we use mostly dimensionless quantities, based on the magnetic field strength of the reconnecting field component in the inflow region B_c, a characteristic density ρ_c, and the ion inertia length $\lambda_i = c/\omega_{pi}$, with other units given by appropriate combinations of these, for instance, velocity $v_c = B_c/\sqrt{\mu_0 \rho_c}$, time $t_c = \lambda_i/v_c = 1/\omega_{ci}$, where $\omega_{ci} = eB_c/m_i$ is the ion cyclotron frequency, pressure $p_c = B_c^2/\mu_0$, and electric field $E_c = v_c B_c$. MHD units were chosen for consistency with the PIC simulation units.

The initial current sheet configuration and the boundary conditions were chosen for comparison with the Newton challenge problem.[14] The initial state consists of a plane current sheet with a profile as in the classical Harris sheet[16]

$$B_x = \tanh(z/L) \quad B_z = 0, \tag{1}$$

with $L=2$, however, also including a guide field. We consider two cases: a uniform guide field and a force-free sheet

$$B_y = B_0 \quad \text{(uniform guide field)}, \tag{2}$$

$$B_y = 1/\cosh(z/L) \quad \text{(force-free field)}, \tag{3}$$

with $B_z = 0$ in both cases. In the force-free case (3) the current is aligned with the magnetic field direction, the magnitude of the total magnetic field is constant, while its direction rotates around the z axis, such that the guide field is unity at $z=0$ and vanishes for large $|z|$. For the PIC simulations we chose a system in which the initial current is carried by the electrons.

The corresponding plasma pressure follows from pressure balance; it is given by

$$p = \frac{1}{2\cosh^2(z/L)} + p_b \quad \text{(uniform guide field)}, \tag{4}$$

$$p = p_0 \quad \text{(force-free field)}, \tag{5}$$

where an arbitrary background pressure $p_b = 0.1$ is included in Eq. (4). The plasma density was chosen as

$$\rho = \frac{1}{\cosh^2(z/L)} + \rho_b \quad \text{(uniform guide field)}, \tag{6}$$

with $\rho_b = 0.2$ and

$$\rho = 1 \quad \text{(force-free field)}, \tag{7}$$

such that the initial temperature was uniform in the constant guide field case.

The boundary conditions include a finite driving period as in the Newton challenge problem,[14] with temporally and spatially localized inflow at $z = \pm L_z$. In the MHD case the inflow speed is given by

$$v_z = \mp \hat{v}(t)\cos^2(\pi x/2L_x) \quad \text{for } z = \pm L_z, \tag{8}$$

$$\hat{v}(t) = d\zeta/dt = 2a\omega \tanh(\omega t)/\cosh^2(\omega t), \tag{9}$$

$$\zeta(t) = a \tanh^2(\omega t). \tag{10}$$

The inflow speed and hence the boundary electric field reach a maximum at $\omega t \approx 0.65$ and subside after $\omega t \approx 2.5$. In the PIC simulations, in addition to the inflow speed, the boundary electric field components E_x and E_y are prescribed in a similar fashion.

The parameters a and ω and the box size, given by $|x| \le L_x$ and $|z| \le L_z$, were also chosen to be the same as in the Newton challenge problem, with

$$a = 2 \quad \omega = 0.2, \qquad L_x = 16 \quad L_z = 8. \tag{11}$$

The PIC simulations are based on a fully electromagnetic PIC code,[17] using 200×400 grid cells with 25 million particles or, in some higher-resolution cases, 400^2 cells in x,z with 250 million particles. Again for comparison with the Newton challenge, a mass ratio $m_i/m_e = 25$ was assumed in most cases. However, to study the influence of this assumption on the results, in one case this ratio was increased to 100. The initial parameters of different PIC runs are listed in Table I. Here β refers to the ratio of plasma to magnetic pressure in the exterior (inflow) region.

In the MHD case, symmetry boundary conditions were employed at $x=0$, $z=0$, and $x=L_x$, a nonuniform grid in z

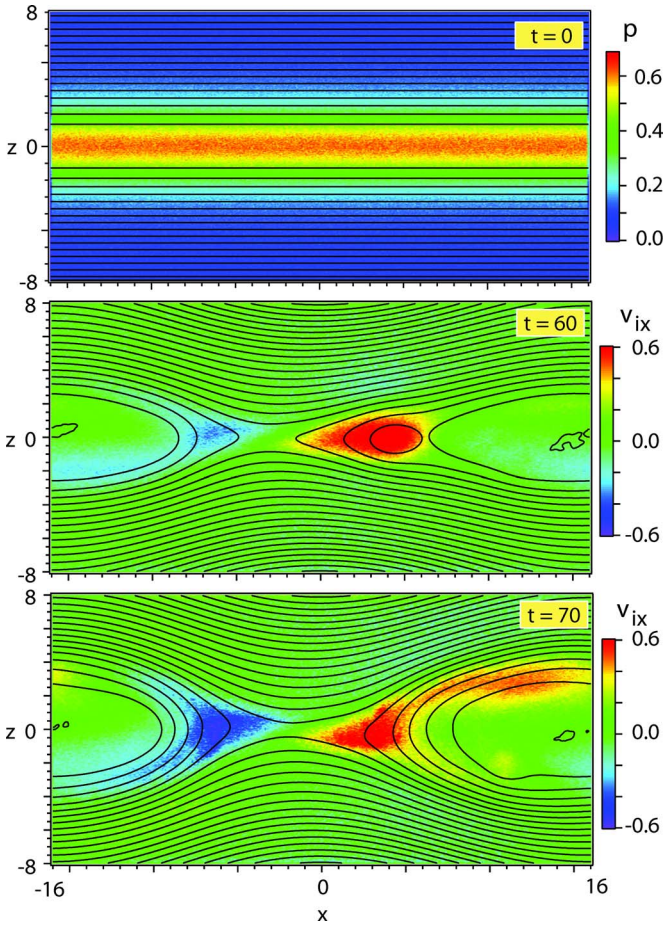

FIG. 1. (Color online) Initial pressure distribution (top) and ion flow speed v_{ix} at two characteristic times for case A1 with initially uniform guide field B_y=0.8, as defined in Table I.

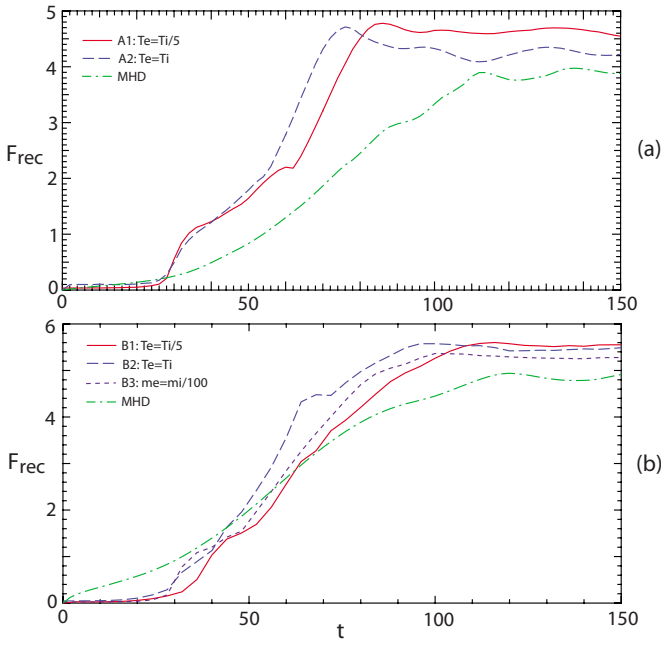

FIG. 2. (Color online) Evolution of the reconnected flux (a) for cases A1 and A2 with initially uniform guide field B_y=0.8 and (b) for cases B1, B2, and B3 starting from a force-free field, as defined in Table I. The corresponding MHD runs are based on localized resistivity defined by Eqs. (12) and (13) with η_{max}=0.05.

was used with about one half of the cells inside the current sheet and up to 200^2 grid cells. A localized resistivity model was given by

$$\eta = \eta_{max}/\cosh^2 r \quad r = \sqrt{(x/s_x)^2 + (z/s_z)^2}, \tag{12}$$

centered at the location of the magnetic null (x-point) $x=0$, $z=0$, where $B_x=0$ and $B_z=0$. Values for η_{max} ranged from 0.005 to 0.5, and the scales for the localized resistivity ("resistive spot") were chosen as

$$s_x = 1 \quad s_z = 1. \tag{13}$$

The grid size and the number of grid points were varied to ensure that they did not affect the results.

III. CHARACTERISTICS OF THE DYNAMIC EVOLUTION

Figure 1 illustrates the characteristic evolution resulting from the forced reconnection for case A1 with initially uniform guide field B_{y0}=0.8, as defined in Table I. The top panel shows the initial pressure distribution (color) and magnetic field lines (black contours). The other two panels show the ion flow velocity component v_{ix} (color) and the magnetic field lines at two different times indicated in the figure. These panels illustrate not only the fast outflow at the time of rapid reconnection but also an asymmetry in x, which occurs frequently in the PIC simulations. This asymmetry may involve a small embedded magnetic island (t=60), which, however, disappears at later times.

The evolution of the reconnected flux (given by the gain in magnetic flux in the outflow, or reduction in magnetic flux in the inflow region) is shown in Fig. 2 for the cases A and B listed in Table I, together with corresponding MHD runs (green dash-dotted lines). Figure 2(a) corresponds to cases A1 and A2 with initially uniform B_y and Fig. 2(b) to initially force-free cases B1, B2, and B3. Figure 2 demonstrates that the ion/electron temperature ratio and the mass ratio have very little influence on the evolution, that is, on the reconnection rate, given by the derivative of the curves, dF_{rec}/dt. The MHD runs exhibit slightly slower growth, due to our choice of relatively modest resistivity with a maximum η_{max}=0.05.

IV. DISSIPATION AND ENERGY TRANSFER

In this section we discuss energy release and transfer based on equations for the individual energy contributions, using a form that is applicable to both MHD and particle simulations. The equations given, for instance, in Ref. 18, are generalized to include heat flux and anisotropic pressure. Electromagnetic energy release and transport is governed by Poynting's theorem (neglecting electric field energy)

$$\frac{\partial}{\partial t}\frac{B^2}{2\mu_0} = -\nabla\cdot\mathbf{S} - \mathbf{j}\cdot\mathbf{E} = -\nabla\cdot\mathbf{S} - \mathbf{j}\cdot\mathbf{E}' - \mathbf{v}\cdot(\mathbf{j}\times\mathbf{B}), \tag{14}$$

where $\mathbf{S}$ is the Poynting vector, denoting (electro)magnetic energy flux

$$\mathbf{S} = \mathbf{E} \times \mathbf{B}/\mu_0, \tag{15}$$

and $\mathbf{E}'$ is the electric field in the plasma rest frame defined by

$$\mathbf{E}' = \mathbf{E} + \mathbf{v} \times \mathbf{B}. \tag{16}$$

In addition there is internal (thermal) energy transport, governed by

$$\frac{\partial u}{\partial t} = -\nabla \cdot [\mathbf{H} + \mathbf{Q}] + \mathbf{v} \cdot (\nabla \cdot \underline{\mathbf{P}}) + \mathbf{j} \cdot \mathbf{E}', \tag{17}$$

where u is the kinetic (quasithermal) energy density in the plasma rest frame defined by the trace of the pressure tensor

$$u = \frac{1}{2}\sum_{j=1}^{3} P_{jj}, \tag{18}$$

and $\mathbf{H}$ denotes enthalpy flux

$$\mathbf{H} = u\mathbf{v} + \underline{\mathbf{P}} \cdot \mathbf{v}, \tag{19}$$

describing not only the convective transport of thermal energy but also contributions from the work of the mechanical stresses $\underline{\mathbf{P}} \cdot \mathbf{v}$, e.g., compression or expansion. $\mathbf{Q}$ represents heat flux and $\underline{\mathbf{P}}$ is the full pressure tensor.

The third form of energy is bulk kinetic energy, governed by

$$\frac{\partial}{\partial t}\frac{\rho}{2}v^2 = -\nabla \cdot \left(\frac{\rho}{2}v^2\mathbf{v}\right) + \mathbf{v} \cdot (\mathbf{j} \times \mathbf{B} - \nabla \cdot \underline{\mathbf{P}}), \tag{20}$$

containing the bulk kinetic energy flux

$$\mathbf{K} = \tfrac{1}{2}\rho v^2 \mathbf{v}. \tag{21}$$

In these equations we have added electron and ion contributions to ease the comparison between PIC and MHD simulations. If the pressure tensor $\underline{\mathbf{P}}$ in Eqs. (17) and (20) is isotropic the term $\mathbf{v} \cdot (\nabla \cdot \underline{\mathbf{P}})$ is replaced by $\mathbf{v} \cdot \nabla p$. However, in general the pressure tensor in particle simulations may not even be gyrotropic. Equations (14), (17), and (20) combined yield the energy conservation law

$$\frac{\partial}{\partial t}\left(u + \frac{1}{2}\rho v^2 + \frac{B^2}{2\mu_0}\right) = -\nabla \cdot (\mathbf{S} + \mathbf{H} + \mathbf{K} + \mathbf{Q}). \tag{22}$$

There are three different terms that govern the transfer of energy from one form to another. The first one is Joule dissipation $\mathbf{j} \cdot \mathbf{E}'$, equivalent to Ohmic heating ηj^2 in the resistive MHD model, providing a transfer from magnetic to internal (thermal) energy. (In the Appendix, we show that this transfer in a two-fluid model involves an intermediate transfer from magnetic to electron kinetic energy.) In the collisionless model that underlies PIC simulations $\mathbf{E}'$ is given by (e.g., Ref. 19)

$$\mathbf{E}' = \frac{1}{ne}\mathbf{j} \times \mathbf{B} - \frac{1}{ne}\nabla \cdot \mathbf{P}_e + \frac{m_e}{ne^2}\left[\frac{\partial \mathbf{j}}{\partial t} + \nabla \cdot (\mathbf{j}\mathbf{v} + \mathbf{v}\mathbf{j})\right]. \tag{23}$$

The first term on the right-hand side of Eq. (23), the Hall term does not contribute to Joule dissipation $\mathbf{j} \cdot \mathbf{E}'$. Therefore the remaining two terms, both of which result from electron inertia, are responsible for collisionless dissipation (e.g., Ref. 20). However, in contrast to Ohmic heating, this term need not be positive everywhere.

The second term, $\mathbf{v} \cdot (\mathbf{j} \times \mathbf{B})$, represents acceleration (or deceleration) by Lorentz forces as a mechanism of transfer between magnetic and bulk kinetic energy, while the third term $\mathbf{v} \cdot (\nabla \cdot \mathbf{P})$ provides the transfer between bulk kinetic energy and thermal energy, representing work done by pressure forces. For isotropic pressure p this term becomes reduced to $\mathbf{v} \cdot \nabla p$. In approximate force balance $\mathbf{j} \times \mathbf{B} \approx \nabla \cdot \mathbf{P}$, the combination of these two terms also provide a mechanism of transfer between magnetic and thermal energy. This is in fact how compressional heating may transfer magnetic to thermal energy also in collisionless plasmas. While this is in principle a reversible process it may contribute to irreversible heating when combined with the unidirectional transport from inflow to outflow in reconnection. We note that the heat flux $\mathbf{Q}$ does not contribute to energy transfer. It acts as a means to redistribute thermal energy, particularly along field lines, where heat conductivity is much larger than across the field.

Examples for the energy outflow in the PIC simulations are shown in Fig. 3 for runs A1 (initially constant B_y, left column) and B1 (initial force-free state, right column), using an initial temperature ratio $T_e/T_i = 1/5$. The results for both cases are quite similar. For a more quantitative evaluation of the relative importance of the transfer terms we have integrated the transfer terms over boxes indicated by the black rectangles in Fig. 3, defining

$$D_J = \int \mathbf{j} \cdot \mathbf{E}' dF, \tag{24}$$

$$D_L = \int \mathbf{v} \cdot (\mathbf{j} \times \mathbf{B}) dF, \tag{25}$$

$$D_P = \int \mathbf{v} \cdot (\nabla \cdot \mathbf{P}) dF, \tag{26}$$

where $dF = dxdz$ and we use Eq. (16) for $\mathbf{E}'$, $\mathbf{j} = ne(\mathbf{v}_i - v_e)$, and the full pressure tensor $\mathbf{P}$. The evaluation was done near the times of fastest reconnection when approximately 1/2 of the total flux was reconnected. The location and size of the boxes were chosen to cover the major inflow and outflow without disturbance from reflected flow. The results for the transfer and the different forms of energy inflow and outflow are listed in Table II for the PIC runs defined in Table I. The last two columns contain the net flux of bulk kinetic energy, $\Delta K = K_{\text{out}} - K_{\text{in}}$ and heat flux, $\Delta Q = Q_{\text{out}} - Q_{\text{in}}$, summed over both particle species which was evaluated only for cases B and C. The column for Joule dissipation (D_J) also contains (in brackets) the dissipation evaluated from the divergence of the electron pressure tensor. The rough consistency with the dissipation evaluated by Eq. (24) not only provides a validity check but also indicates that the inertia term in Eq. (23) contributes less to dissipation than the pressure term. This is consistent with earlier findings about the dissipation in guide field reconnection.[10]

Table II demonstrates the following features:

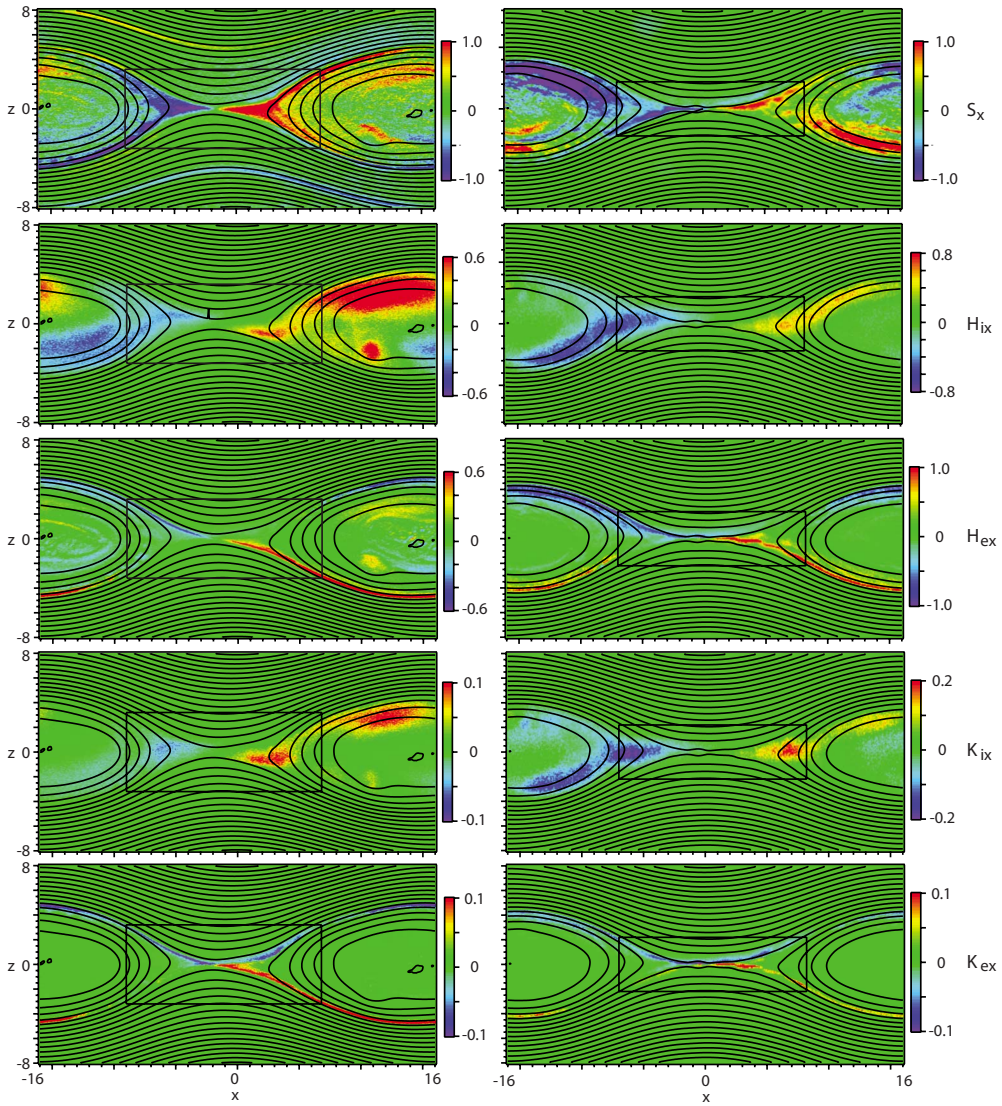

FIG. 3. (Color online) Energy outflow for PIC simulations A1 (left) and B1 (right) near the time of fastest reconnection, showing (from top to bottom) Poynting flux S_x, ion enthalpy flux H_{ix}, electron enthalpy flux H_{ex}, ion bulk kinetic energy flux K_{ix}, and electron bulk kinetic energy flux K_{ex}. Black rectangles indicate the boundaries of boxes used to integrate incoming and outgoing energy fluxes discussed in Sec. IV.

(1) The net heat fluxes into or out of the box ΔQ (summed over both particle species), which are evaluated here only for the force-free cases, are relatively small. This shows that the energy generated by Joule heating or compressional heating is not carried away by thermal conduction.
(2) The net outgoing bulk kinetic energy fluxes ΔK (again summed over both particle species) are also small com-

TABLE II. Dissipation and energy transfer for the runs listed in Table I. D_J denotes Joule dissipation, defined by Eq. (24); D_L is the transfer by Lorentz forces (25); D_P the work done by pressure gradient forces (26); S the magnetic energy (Poynting) flux, defined by Eq. (15); and H enthalpy flux (19). The last two columns contain the net flux of bulk kinetic energy $\Delta K = K_{\text{out}} - K_{\text{in}}$, Eq. (21), and heat flux, $\Delta Q = Q_{\text{out}} - Q_{\text{in}}$, summed over both particle species. The latter was evaluated only for cases B and C.

Case	D_J	D_L	D_P	S_{in}	S_{out}	$H_{i,\text{in}}$	$H_{i,\text{out}}$	$H_{e,\text{in}}$	$H_{e,\text{out}}$	ΔK	ΔQ
0	0.48(0.30)	1.46	1.43	2.03	0.69	0.59	2.46	0.24	0.79	0.31	⋯
A1	0.61(0.72)	1.48	1.57	5.69	5.24	0.62	2.87	0.13	0.85	0.19	⋯
A2	0.62(0.93)	1.36	1.60	5.11	5.69	0.38	1.82	0.22	1.56	0.04	⋯
B1	1.48(2.16)	1.94	2.05	4.36	3.86	1.15	2.46	0.28	2.00	0.33	0.29
B2	0.97(1.75)	2.01	2.39	4.28	3.09	0.72	1.98	0.96	2.45	0.23	0.10
B3	1.00(1.34)	1.95	2.01	4.69	4.59	1.12	3.03	−0.02	0.95	0.83	−0.09
C	0.12(0.37)	0.47	0.50	0.19	0.89	0.18	1.93	0.24	0.69	0.07	−0.04

pared to the other energy fluxes, despite the fact that acceleration by Lorentz forces provides a significant transfer from magnetic to kinetic energy D_L. The reason is the approximate balance between the effects of the Lorentz forces (D_L) and pressure gradient forces (D_P), such that the transferred energy leads to compressional heating and an increase in enthalpy flux H, rather than bulk acceleration.

(3) Joule heating (D_J), which is relatively small in case 0 without guide field, is somewhat larger in the guide field cases, although still smaller than the adiabatic transfer ($D_L \approx D_P$). The probable reason is the fact that, in the presence of a strong guide field, particles can stay longer in the acceleration region close to the separator line, experiencing more acceleration and providing larger current density and thereby larger Joule dissipation.

(4) As to be expected, in the presence of a guide field, a significant (even dominant) portion of the incoming magnetic energy (Poynting) flux simply becomes redirected.

(5) There is approximate balance between the heating terms (D_J+D_P) and the gain in enthalpy flux ($H_{\rm out}-H_{\rm in}$). This indicates that the energy transferred to heat is not deposited but results in the increase in enthalpy flux.

(6) In contrast, reduction in Poynting flux ($S_{\rm out}-S_{\rm in}<0$) does not balance the transfer from magnetic to kinetic energy ($-D_J-D_L$). This shows that the systems are not in a steady state and that the magnetic energy within the box decreases. This is related to the fact that the compression that is mainly responsible for the increase in the enthalpy flux also causes an increase of the guide field, such that the outgoing Poynting flux carries larger guide field than the incoming flux. In the initially force-free cases (B and C) this is enhanced by the fact that the guide field strength decreases in time in the inflow region as reconnection proceeds.

(7) A significant portion of the energy transfer goes to electron enthalpy flux ($H_{e,\rm out}$), even when the electrons initially are much colder than the ions (cases A1, B1, B3, and C). However, this effect decreases somewhat for more realistic electron mass (case B3).

(8) Reducing the electron/ion mass ratio, however, has no significant effect on dissipation and overall energy transfer properties, as shown by comparison between cases B2 and B3.

(9) High β in the inflow region (case C) reduces energy transfer rates. As we will see in Sec. V, this also affects the amounts of energy and magnetic flux released.

V. LATE STATES AND GLOBAL CONSTRAINTS

At late times the simulations approach near-equilibrium configurations. The results are illustrated in Fig. 4 for initially uniform B_y (PIC simulation A1) and Fig. 5 for initially force-free fields (PIC simulation B1). The PIC results are shown in the left columns and the corresponding MHD results in the right columns. Figures 4 and 5 show, from top to bottom, (a) the density ρ, (b) the pressure p, given by the trace of the pressure tensor

$$p = \frac{1}{3}\sum_{j=1}^{3} P_{jj}, \tag{27}$$

and the sum of electron and ion pressures in the PIC case, (c) the magnetic field component B_y, (d) the current density component J_y, and (e) the temperature given by $T=p/\rho$.

Overall, Figs. 4 and 5 show very good agreement between PIC and MHD results, demonstrating the same characteristic features. Note particularly the characteristic exchange in the roles of plasma pressure p and the magnetic field component B_y (or its corresponding pressure contribution) between Figs. 4 and 5. In the case of initially uniform B_y (Fig. 4), the pressure becomes concentrated nearly uniformly in the center of the magnetic islands formed by reconnection, while B_y (as well as the current density J_y) are enhanced in rings around this center. The opposite is the case for the initially force-free case (Fig. 5) whereas the current density J_y maintains the same ring structure. This behavior is understandable from the fact that in 2.5-dimensional equilibrium, the current density J_y is given by

$$J_y = \frac{d}{dA}\left[p(A) + \frac{B_y^2(A)}{2\mu_0}\right], \tag{28}$$

where indeed plasma pressure $p(A)$ and magnetic pressure $B_y^2(A)/2\mu_0$ play interchangeable roles. Here A represents the flux function or y component of the vector potential, defining the magnetic field via

$$\mathbf{B} = \nabla A \times \hat{\mathbf{y}} + B_y\hat{\mathbf{y}}, \tag{29}$$

where $\hat{\mathbf{y}}$ is the unit vector in the y direction.

The similarities between the late PIC and MHD results in Figs. 4 and 5 suggest that these configurations are governed, at least approximately, by integral conservation laws similar to those identified in the case without guide field.[21] For 2.5-dimensional ideal MHD configurations, when the magnetic field is given by Eq. (29) and a gauge is chosen in which the A value is conserved within a moving plasma element, one can identify (e.g., Ref. 15) mass conservation

$$M = \int \rho ds/B = M(A), \tag{30}$$

conservation of an entropy function

$$S = \int p^{1/\gamma} ds/B = S(A), \tag{31}$$

and when footpoints of field lines are fixed at the boundary, the footpoint displacement

$$Y = \int dy = \int B_y ds/B = Y(A), \tag{32}$$

which can be related to magnetic helicity.[15] The integration in Eqs. (30)–(32) is extended along each field line from one boundary footpoint to the other and field lines that close within the box are excluded.

These conservation laws are based on ideal MHD. As discussed by Birn *et al.*,[15] they can be generalized, however, to allow for changes in topology, provided that nonideal

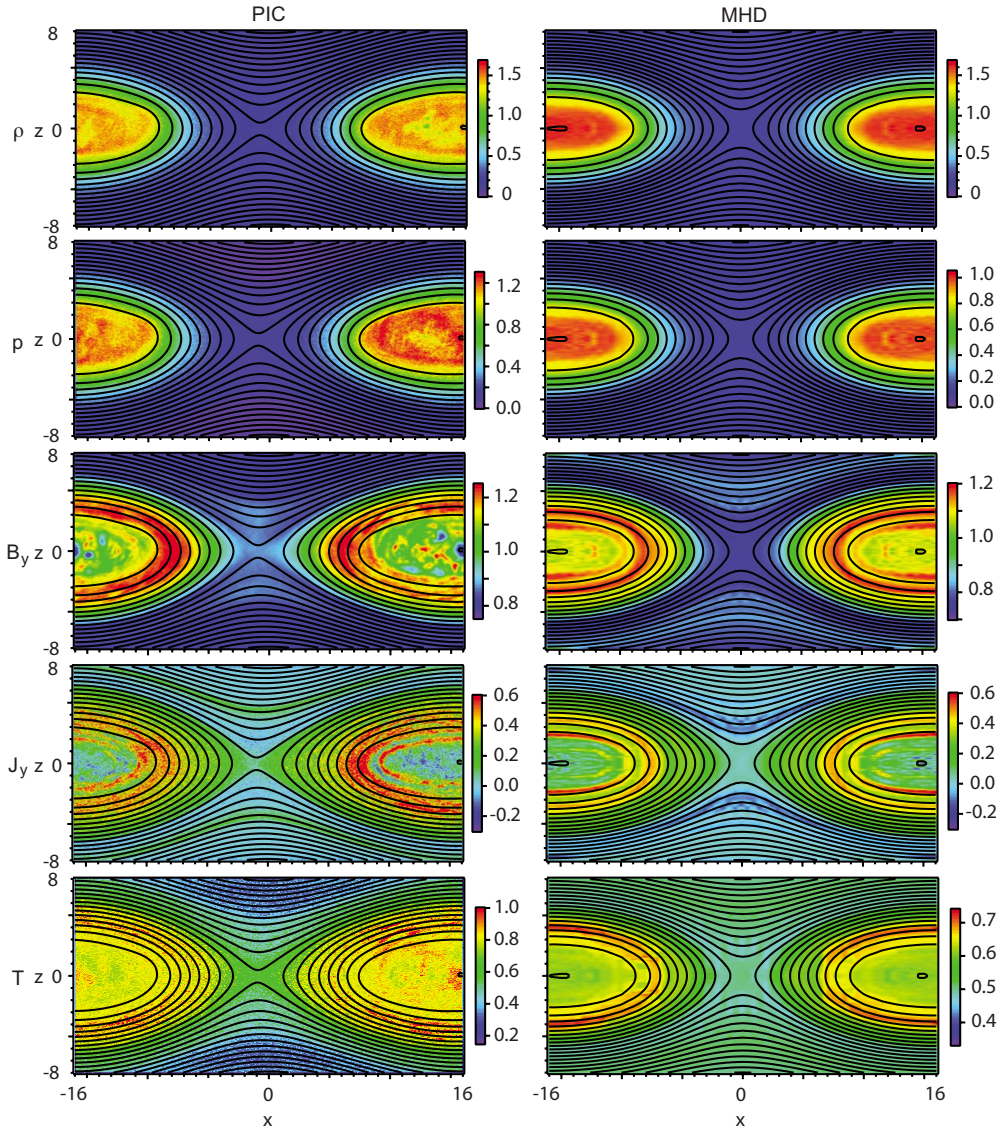

FIG. 4. (Color online) Late configurations of runs with initially uniform $B_y=0.8$: (left) PIC simulation A1 (Table I) at $t=160$, (right) corresponding MHD simulation at $t=400$ with $\eta_{max}=0.005$. From top to bottom: density ρ, pressure p, the magnetic field component B_y, the current density component J_y, and the temperature given by $T=p/\rho$.

MHD effects are strongly localized. In symmetric configurations, such as considered here, the segments of magnetic flux tubes that become newly connected should have equal amounts of mass and entropy so that the sums remain the same as before reconnection. In the PIC simulations, this symmetry might be violated at intermediate states (e.g., Fig. 1) but it is well satisfied at late stages, as demonstrated by Figs. 4 and 5.

To investigate the validity of the conservation laws, we have evaluated mass M, entropy S, and displacement Y as functions of A by numerically integrating Eqs. (30)–(32) for both, PIC and MHD, simulations. Figures 6 and 7 show the results for cases A1 (initially constant B_y) and B1 (force-free initial state), respectively. Red (dash-dotted) lines represent PIC results and blue (solid) lines the corresponding MHD results while the dashed lines show the initial functions. The top rows show, from left to right, M, Y, and S, and the bottom rows density ρ, magnetic field component B_y, and pressure p. For the PIC simulation the pressure p was again defined by the trace of the full pressure tensor, given by Eq. (27). However, using $p=p_{\parallel}^{1/3}p_{\perp}^{2/3}$, suggested by double-adiabatic theory, instead made no visible difference.

The mass and displacement functions $M(A)$ and $Y(A)$ in Figs. 6 and 7 show remarkable agreement with each other and with the initial distribution, despite the fact that most field lines at the late times have undergone reconnection. This demonstrates the absence of slippage. The entropy functions $S(A)$ for the PIC simulations show a slight increase which is more pronounced in the initially force-free PIC case B1 (top right panel of Fig. 7). This indicates that Joule dissipation at the reconnection site provides somewhat larger nonadiabatic heating than in the case without guide field.[21] This is consistent with the dissipation rates listed in Table II. The relatively larger entropy increase in the force-free case is probably due to the fact that this case has initially lower plasma pressure inside the current sheet, such that a pressure enhancement from nonadiabatic heating causes a larger rela-

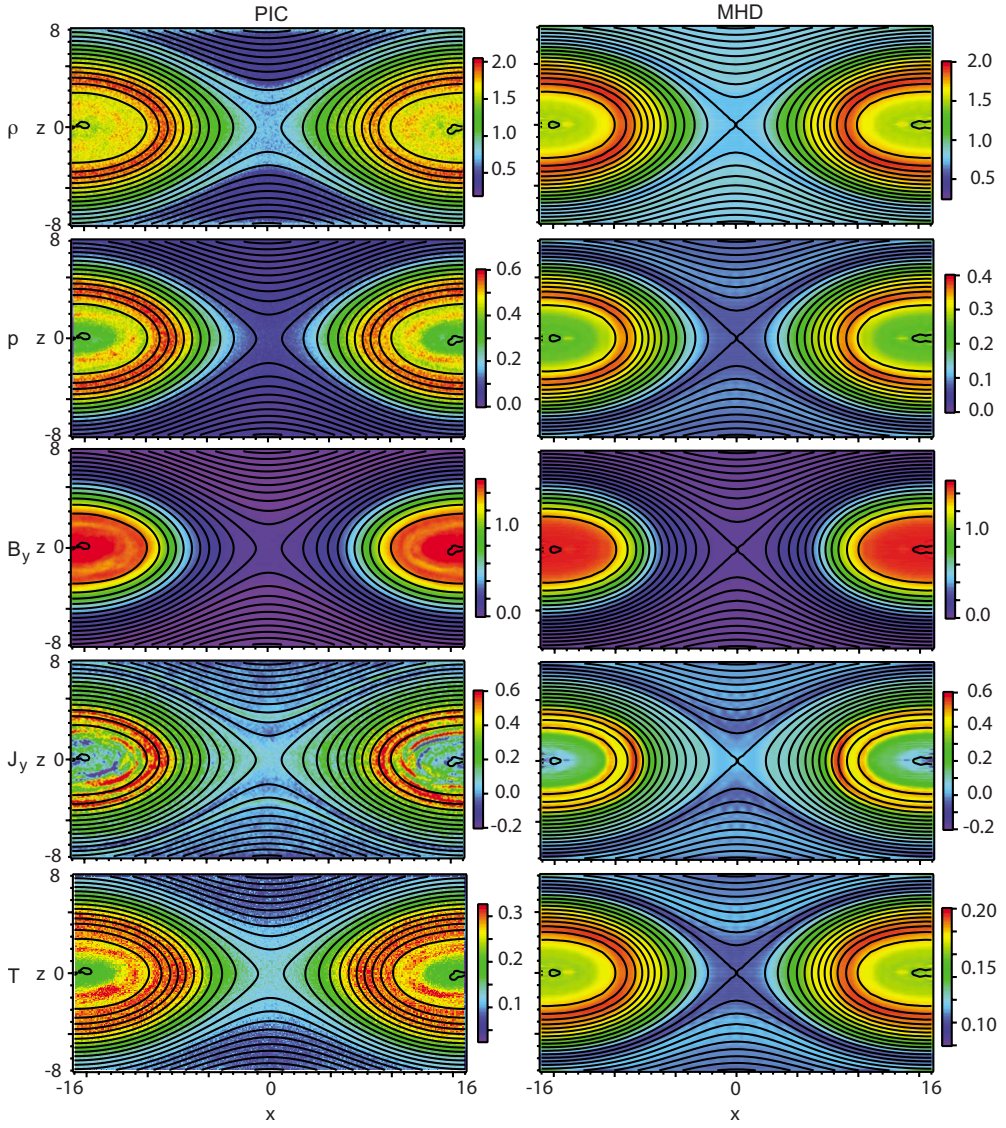

FIG. 5. (Color online) Same as Fig. 4 but for initially force-free fields B1 (PIC) and a corresponding MHD run with $\eta_{max}=0.005$.

tive change in pressure and entropy. We note that some differences in the pressure functions $P(A)$ are also due to the fact that the PIC simulations have evolved slightly more than the MHD simulations. This can be inferred from the small local peaks visible in $M(A)$ and $S(A)$, as discussed below. The guide field functions $B_y(A)$ in Figs. 6 and 7 change considerably from the initial functions. The basic changes are similar for MHD and PIC; however, the late functions in Fig. 6 differ somewhat quantitatively, in part also due to the fact that the PIC simulation has proceeded farther, i.e., reconnected more flux.

We note that $M(A)$, $Y(A)$, and $S(A)$ should diverge at the separatrix when the B-field remains regular. This is related to the fact that the flux tube volume per unit magnetic flux

$$V=\int ds/B, \tag{33}$$

diverges logarithmically on field lines approaching a regular x-line or separator, where the (poloidal) magnetic field goes to 0 linearly. This singularity is evidenced by the local peaks in Figs. 6 and 7, thus indicating the flux value at the x-point. In the PIC simulation this location has proceeded to slightly larger values of $|A|$.

In Fig. 6, case A, the entropy curve for the MHD case (blue solid line, top right panel) shows a similar increase as the curve for the PIC case (red dash-dotted line), whereas the MHD entropy function agrees better with the initial one in case B (Fig. 7). This result stems mainly from our choice of a wider resistive spot in x in case A, using $s_x=4$ and $s_z=2$ instead of Eq. (13) with $\eta_{max}=0.0025$. This influence can be simply understood from the total dissipation, which is given approximately by $E_r J_y d_x d_z$, where E_r is the reconnection rate (electric field at the reconnection site), J_y is the current density, approximately given by $J_y \approx \partial B_x/\partial z$, and d_x and d_z are the widths of the dissipation region in x and z, respectively. In our case, the width of the resistive spot is wider than the current layer at the reconnection site. Therefore d_z is essentially given by the half-width of this current layer, such that $J_y d_z \approx B_x$, the magnetic field just outside the dissipation region which is of order unity. If we assume that fast recon-

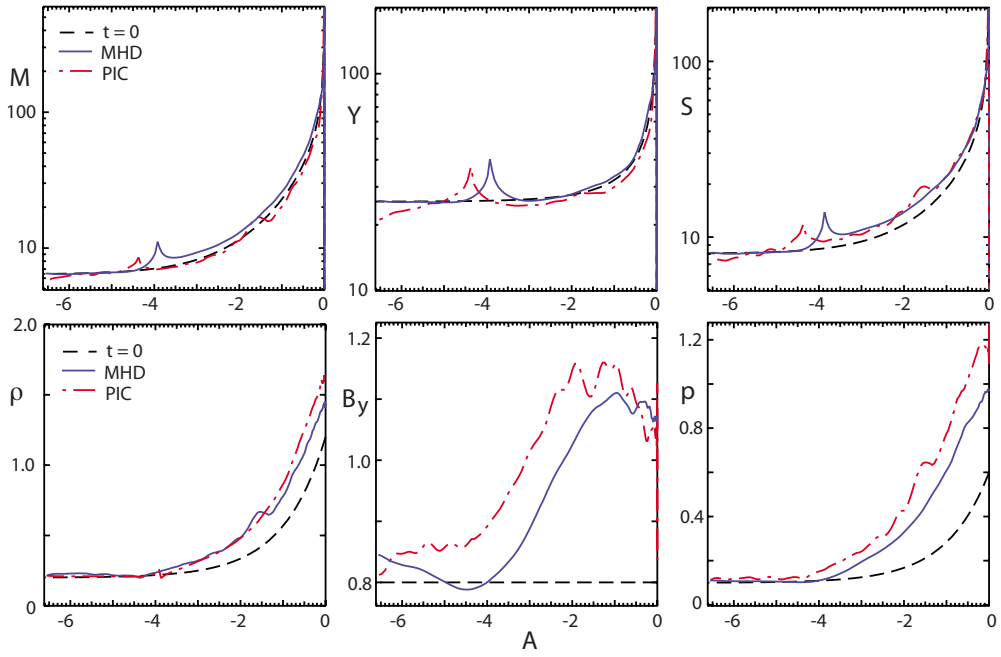

FIG. 6. (Color online) Integral quantities at late times as functions of A for the cases with initially constant B_y. The top row shows, from left to right: mass M, footpoint displacement Y, and entropy function S for PIC run A1 (red dashed-dotted lines) and MHD (blue solid lines) with $\eta_{max}=0.0025$, using $s_x=4$ and $s_z=2$ instead of Eq. (13). The bottom row shows, from left to right: density ρ, magnetic field component B_y, and pressure p.

nection operates at a maximum rate of 0.1 (normalized by the reconnecting magnetic field in the inflow region B_x and an Alfvén speed v_A), then the total Joule dissipation depends only on the length of the dissipation region d_x. In our MHD simulations we did not quite reach the maximum rate; therefore there is still a small dependence on η such that the total Ohmic dissipation becomes smaller when η gets smaller.

VI. ANISOTROPY

In the previous sections we have focused primarily on properties that can be compared between PIC and MHD simulations. In this section we look at features that are not obtainable in MHD, specifically the evolution of anisotropy and characteristics of the distribution functions responsible

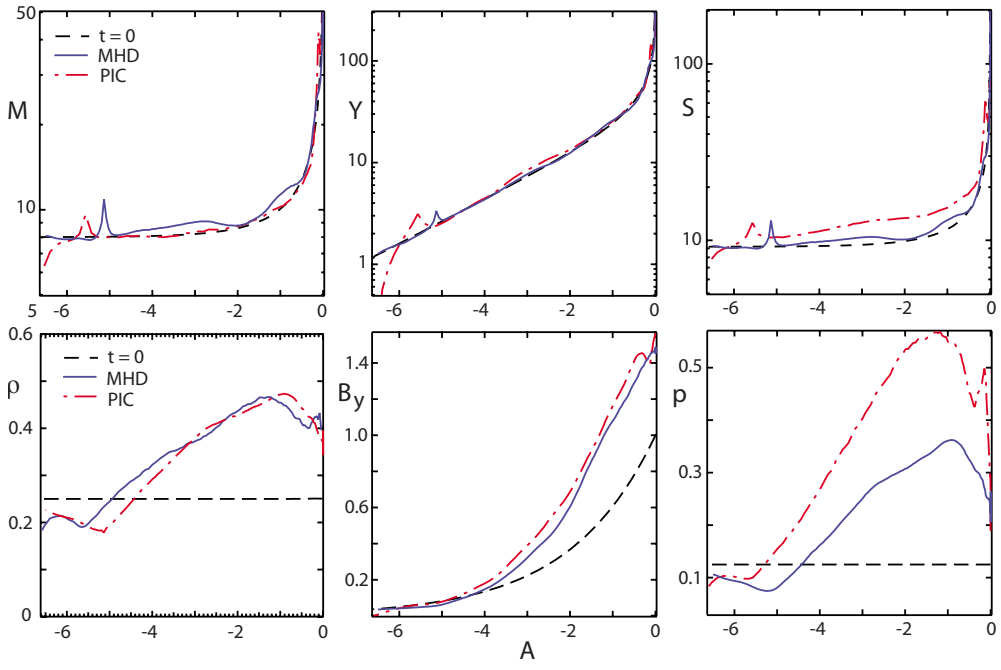

FIG. 7. (Color online) Same as Fig. 6 but for the initially force-free cases B1 (PIC) and MHD with $\eta_{max}=0.005$.

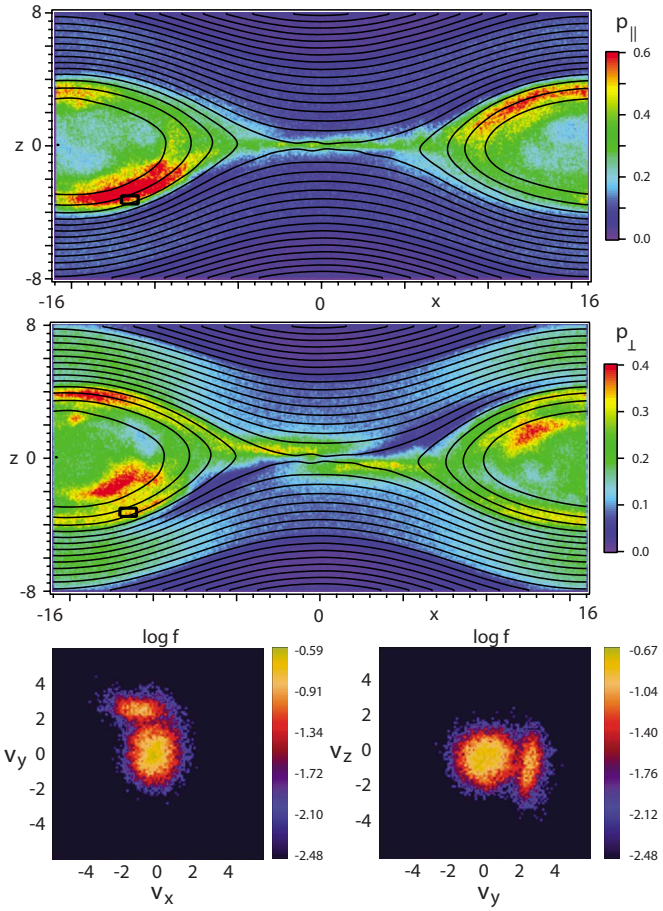

FIG. 8. (Color online) Ion pressure components parallel (top) and perpendicular (center) to the magnetic field and ion velocity distributions (bottom) integrated over the black rectangle indicated in the top panels at $t=60$, for the force-free initial case B1.

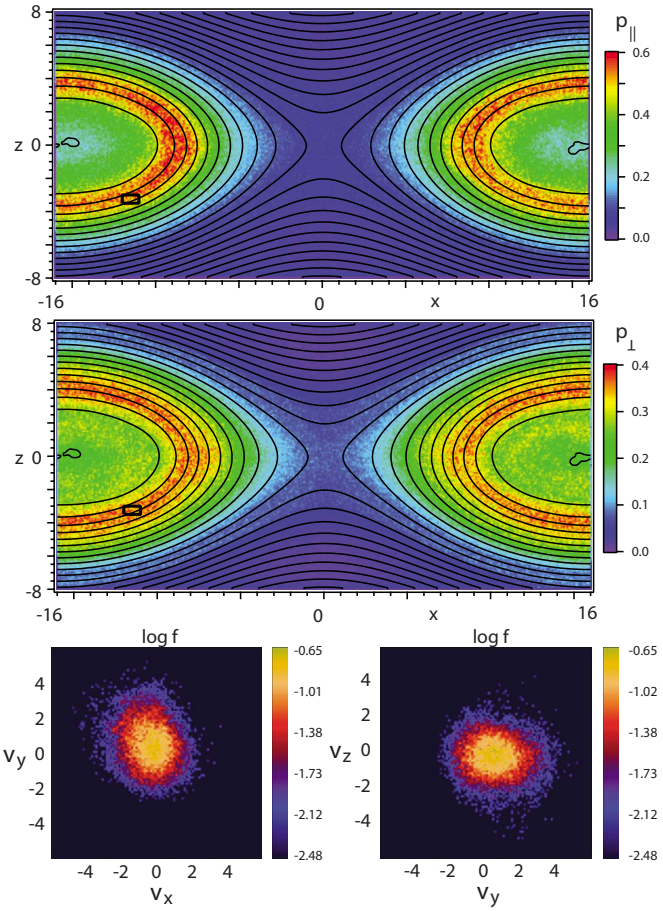

FIG. 9. (Color online) Same as Fig. 8 but at $t=176$.

for the anisotropies. Figures 8 and 9 show the ion pressure components parallel (top) and perpendicular (center) to the magnetic field, together with cuts through the ion velocity distributions (bottom panels) in the outflow region [black rectangles in Figs. 8(a), 8(b), 9(a), and 9(b)], at the time of the fastest reconnection, $t=60$, and for the late, near-equilibrium state, $t=176$, respectively. The figures demonstrate considerable anisotropies. Furthermore, Fig. 8(c) shows that what appears as anisotropy in the outflow in Figs. 8(a) and 8(b) is actually the result of a two-component population. One, more isotropic, component is apparently the population directly convected across the separatrix without encountering the acceleration site, whereas the other, more field-aligned component shows the effects of acceleration along the magnetic field. At later times, however, the two populations mix and become more appropriately describable as anisotropic.

VII. SUMMARY AND CONCLUSIONS

Using PIC and resistive MHD simulations, we have investigated effects of a guide field on reconnection in a scenario akin to the "Newton challenge" problem,[14] in which a plane current sheet is deformed by nonuniform external inflow over a limited time. Despite strong anisotropies in the PIC simulations and differences between electron and ion behavior, MHD and PIC simulations agreed in several important aspects:

1. The outgoing bulk kinetic energy fluxes are insignificant in comparison to the fluxes of electromagnetic (Poynting) and thermal (enthalpy flux) energy.
2. The conversion of magnetic energy to enthalpy flux results from an approximate force balance between pressure gradient and Lorentz forces for the outflow into a closed region. (We note that this result is different when the outflow is into an open region, such as the region above the reconnection site associated with flares in the solar corona or tailward of the reconnection site in the geomagnetic tail for magnetospheric substorms.)
3. Direct Joule dissipation is less significant than quasiadiabatic heating. This does not change with more realistic electron mass and does not significantly depend on the dissipation mechanism, at least in the regime of fastest reconnection. This can be simply understood from the total dissipation, given approximately by $E_r J_y d_x d_z$, where E_r is the reconnection rate (electric field at the reconnection site), J_y is the current density, and d_x and d_z are the widths of the dissipation region in x and z, respectively. Using $J_y \approx \partial B_x/\partial z \approx B_x/d_x$ and assuming that

fast reconnection operates at a (normalized) maximum rate of 0.1 the total joule dissipation depends only on the length of the dissipation region d_x. However, for very large d_x the reconnection rate is expected to go down.

4. The local PIC and MHD simulations are consistent with large-scale three-dimensional MHD simulations in that the released energy goes primarily to redirected Poynting flux and enthalpy flux. For $T_i = T_i$ in inflow region ion and electron outgoing enthalpy fluxes are similar. But even for $T_e < T_i$ stronger electron heating makes the two comparable.
5. The final states approached in MHD and PIC simulations are quite similar. This results from the fact that the global constraints governing MHD are approximately satisfied also by the PIC simulations, at least on the Alfvénic time scales considered here. This is surprising considering that the PIC simulations showed anisotropies, asymmetries, and differences between ions and electron energy fluxes not included in MHD.

ACKNOWLEDGMENTS

This work was performed under the auspices of the U.S. Department of Energy, supported by NASA's Heliophysics Theory, Living With a Star, and SR&T Programs, and through a grant from NASA's MMS/SMART program.

APPENDIX: RELATIONSHIP BETWEEN ONE-FLUID AND TWO-FLUID DISSIPATION

In Sec. IV we have discussed energy transfer, conversion, and dissipation on the basis of one-fluid equations, for an easier comparison between PIC and MHD results. In that formulation the term $\mathbf{j}\cdot\mathbf{E}'$ provides a direct transfer from magnetic energy, governed by Eq. (14), to thermal energy, governed by Eq. (17). In a two-fluid model, however, this energy transfer, which may be interpreted as Joule dissipation, is more complicated. The energy equations for two species equivalent to Eq. (17) are

$$\frac{\partial u_s}{\partial t} = -\nabla\cdot[u_s\mathbf{v}_s + \underline{\mathbf{P}}_s\cdot\mathbf{v}_s + \mathbf{Q}_s] + \mathbf{v}_s\cdot(\nabla\cdot\underline{\mathbf{P}}_s) \quad s = i,e. \tag{A1}$$

In addition there are two equations of motion for ions and electrons

$$n_s m_s \frac{d\mathbf{v}_s}{dt} = -\nabla\cdot\underline{\mathbf{P}}_s + n_s q_s(\mathbf{E}+\mathbf{v}_s\times\mathbf{B}) \quad s = i,e. \tag{A2}$$

We note that the moments in Eqs. (A1) and (A2) are defined in the individual rest frames. We now see that the energy transfer term $\mathbf{j}\cdot\mathbf{E} = (n_i q_i \mathbf{v}_i + n_e q_e \mathbf{v}_e)\cdot\mathbf{E}$ provides a transfer to both ion and electron momentum balances. However, electron momentum balance, which constitutes the generalized Ohm's law, is typically dominated by the balance between the electric field in the electron rest frame and the divergence of the electron pressure tensor. This term then provides a further transfer to internal energy. Here we have discussed this dissipation mechanism just on the basis of the leading terms. An exact derivation of the one-fluid [Eq. (17)] requires the inclusion of all terms and the distinction between the one-fluid moments, defined on the basis of the common rest frame and the individual moments based on the individual rest frames.

[1] H. P. Furth, J. Killeen, and M. Rosenbluth, Phys. Fluids **6**, 459 (1963).
[2] H. E. Petschek, in *Proceedings of the AAS/NASA Symposium on the Physics of Solar Flares, NASA SP-50*, 1964, edited by W. N. Hess (NASA, Washington, DC, 1964), pp. 425–439.
[3] D. Biskamp, *Magnetic Reconnection in Plasmas* (Cambridge University Press, Cambridge, 2000).
[4] B. N. Rogers, R. E. Denton, and J. F. Drake, J. Geophys. Res. **108**, 1111, doi:10.1029/2002JA009699 (2003).
[5] R. Fitzpatrick and F. Porcelli, Phys. Plasmas **11**, 4713 (2004).
[6] P. Ricci, J. U. Brackbill, W. Daughton, and G. Lapenta, Phys. Plasmas **11**, 4102 (2004).
[7] J. D. Huba, Phys. Plasmas **12**, 012322 (2005).
[8] P. L. Pritchett, Phys. Plasmas **12**, 062301 (2005).
[9] P. A. Cassak, J. F. Drake, and M. A. Shay, Phys. Plasmas **14**, 054502 (2007).
[10] M. Hesse, M. Kuznetsova, K. Schindler, and J. Birn, Phys. Plasmas **12**, 100704 (2005).
[11] B. P. Sullivan, B. N. Rogers, and M. A. Shay, Phys. Plasmas **12**, 122312 (2005).
[12] M. Swisdak, J. F. Drake, M. A. Shay, and J. G. McIlhargey, J. Geophys. Res. **110**, A05210, doi:10.1029/2004JA010748 (2005).
[13] W. Wan, G. Lapenta, G. L. Delzanno, and J. Egedal, Phys. Plasmas **15**, 032903 (2008).
[14] J. Birn, K. Galsgaard, M. Hesse, M. Hoshino, J. Huba, G. Lapenta, P. L. Pritchett, K. Schindler, L. Yin, J. Büchner, T. Neukirch, and E. R. Priest, Geophys. Res. Lett. **32**, L06105, doi:10.1029/2004GL022058 (2005).
[15] J. Birn, M. Hesse, K. Schindler, and S. Zaharia, J. Geophys. Res. **114**, A00D03, doi:10.1029/2008JA014015 (2009).
[16] E. G. Harris, Nuovo Cimento **23**, 115 (1962).
[17] M. Hesse, J. Birn, and M. Kuznetsova, J. Geophys. Res. **106**, 3721, doi:10.1029/1999JA001002 (2001).
[18] J. Birn and M. Hesse, Ann. Geophys. **27**, 1067 (2009).
[19] V. M. Vasyliūnas, Rev. Geophys. Space Phys. **13**, 303, doi:10.1029/RG013i001p00303 (1975).
[20] M. Hesse, in *Reconnection of Magnetic Fields: MHD and Collisionless Theory and Observations*, edited by J. Birn and E. R. Priest (Cambridge University Press, Cambridge, 2007), p. 108.
[21] J. Birn, M. Hesse, and K. Schindler, Phys. Plasmas **13**, 092117 (2006).